

Nonlinear spectroscopy of excitonic states in transition metal dichalcogenides

Vyacheslav D. Neverov,^{1,2} Alexander E. Lukyanov,^{1,2} Yaroslav V. Zhumagulov,^{3,2}
Dmitry R. Gulevich,² Andrey V. Krasavin,¹ Alexei Vagov,² and Vasili Perebeinos⁴

¹*National Research Nuclear University MEPhI, Moscow 115409, Russian Federation*

²*ITMO University, St. Petersburg 197101, Russian Federation*

³*University of Regensburg, Regensburg 93040, Germany*

⁴*Department of Electrical Engineering, University at Buffalo,
The State University of New York, Buffalo, New York 14260, USA*

(Dated: September 27, 2021)

Second-harmonic generation (SHG) is a well-known nonlinear spectroscopy method to probe electronic structure, specifically, in transition metal dichalcogenide (TMDC) monolayers. This work investigates the nonlinear dynamics of a strongly excited TMDC monolayer by solving the time evolution equations for the density matrix. It is shown that the presence of excitons qualitatively changes the nonlinear dynamics leading, in particular, to a huge enhancement of the SHG signal at exciton resonances. It is also shown that the SHG polarization angular diagram and its dependence on the driving strength are very sensitive to the type of the exciton state. This sensitivity suggests the SHG spectroscopy is a convenient tool for analyzing the fine structure of excitonic states.

I. INTRODUCTION

Second-harmonic generation (SHG) [1] is a powerful tool for studying optical properties of a variety of materials, including semiconductors [2–4], molecules [5], carbon nanotubes [6–8], and layered transition metal dichalcogenide (TMDC) structures [9–26]. The nonlinear nature of the SHG allows probing material characteristics on a level that usually evades linear spectroscopy methods. For example, the sensitivity of SHG measurement to spatial and time-reversal symmetries makes it handy for uncovering phenomena out of reach of more traditional optical methods [27], including magnetic ordering [28, 29] and hidden phase transitions [30]. Recently the SHG spectroscopy has been applied to map the strain profile with the spatial resolution surpassing the optical diffraction limit [19, 20].

In TMDC monolayers [31], the SHG method has been applied to investigate symmetry of the crystal structure [9–13, 22, 32], detect charged molecules [33], map strains [19, 20, 25], and probe the valley polarization [26, 34, 35]. The SHG signal is very sensitive to electronic excitations, making it a powerful tool for studying the band structure and inter-band transitions. The SHG is a unique tool to fill the gap left by the Raman and photoluminescence spectroscopy, and it is well suited to study atomic and electronic structures of 2D layered TMDC systems [24]. Experiments with layered WSe₂ on h-BN substrates [23], WS₂ [14], MoS₂ monolayers [19] and bilayers [15], and 2D GaSe crystal [36] revealed a conventional six-leaf pattern of the SHG signal angular dependence, which is commonly employed to determine the orientation of the monolayer crystals [9–13, 22, 32]. Distortions of that symmetry, e.g., by an applied tensile strain, give rise to a distorted SHG angular dependence [20].

We show here that the SHG signal’s sensitivity to the excitation field intensity, frequency, and polarization

can be used to probe the nature of electronic states in TMDC materials on a much more detailed level than linear spectroscopy allows. Unlike the linear response spectra, the interpretation of the SHG signals involves theoretical analysis that cannot be limited to calculating the transition energies and rates but requires one to investigate the nonlinear dynamics of the system, which is a much more complex problem. In some cases, the analysis can be simplified by employing the dynamical perturbation theory to calculate the second harmonic. However, the perturbative approach fails in a most physically interesting case of strong excitations and highly nonlinear dynamics or when the higher-order harmonics are essential. It is also not convenient when one has a mixture of excitations of different nature. In those cases, the complete nonlinear dynamical problem must be solved. For TMDC monolayers, it is often solved for single-particle excitations treated within the semi-classical approximation. This approach is well justified, e.g., when the driving field of extra-strong intensity produces many high harmonics.

In many other relevant situations, such as SHG, the field strength is not strong enough to ionize excitons, and single-particle approximation may become inadequate, although the dynamics is still nonlinear. In 2D materials, this regime is easily accessible because of the strong Coulomb interaction enhancing the many-body effects. It facilitates the formation of tightly bound many-particle excitonic complexes, manifested in the linear optical spectra of 2D TMDC structures [37–42]. The exciton-related effects should also be visible in nonlinear dynamics, in particular, SHG. However, investigations of the nonlinear dynamics associated with the excitonic states are currently in the infant stage. Contemporary research focuses mainly on the linear response [43–50]. Analysis of the nonlinear effects such as SHG mainly concentrates on perturbative calculations [51, 52]. A more elaborate investigation of the exciton dynamics in TMDC can be done by solving dynamics equations for the per-

inent elements of the density matrix [53] obtained using the dynamics control truncation (DCT) approximation [54].

In this work, we investigate the role of exciton states in the SHG of TMDC monolayers. Using the solution for the Liouville - von Neumann (LvN) equation, we obtain SHG angular polarization diagrams and study their dependence on the frequency and intensity of the excitation pulse. The results reveal an extraordinary sensitivity of the SHG signal on the type of exciton states. Our findings are general, and similar SHG polarization diagrams are obtained for monolayers of common TMDC's (MoS₂, MoSe₂, WS₂, and WSe₂) with a qualitatively similar two valley band structure. Our results offer a tantalizing possibility for the SHG spectroscopy of exciton states that can be used to probe and detect finer details of excitonic states that conventional optical methods cannot capture.

II. DYNAMICS OF EXCITON STATES

The analysis of the harmonic generation is done by employing the formalism of the density matrix where we solve the LvN equation,

$$\frac{d\rho}{dt} = -\frac{i}{\hbar} [H, \rho] + \mathcal{L}[\rho], \quad (1)$$

where ρ is the density matrix, H is the Hamiltonian of the system, and \mathcal{L} is introduced to account for losses, for which we assume the form of the Lindblad operator. Since we are interested in the exciton contribution to the dynamics, we consider the two-particle Hamiltonian. It contains two contributions $H = H_{ex} + H_f$ where H_{ex} is the part describing the exciton states, and H_f is the interaction between the excitons and the driving field. The LvN equation is solved using a basis of two-particle exciton eigenstates, which are in turn calculated using conduction and valence band single-particle states of a TMDC material as a basis.

A. Single-particle states

Single-particle states are obtained from the massive Dirac model Hamiltonian, which takes into account the trigonal warping and spin-orbit coupling [55–57]. It yields a good approximation for the low-lying states of a TMDC monolayer. The Hamiltonian reads as

$$\begin{aligned} H_0(\mathbf{k}) = & \frac{\Delta}{2} \sigma_z + \hbar v_F \tau (k_x \sigma_x + \tau k_y \sigma_y) \\ & + \frac{\tau s}{2} \{ \lambda_c (\sigma_z + \sigma_0) - \lambda_v (\sigma_z - \sigma_0) \} \\ & + \kappa \{ (k_x^2 - k_y^2) \sigma_x + 2\tau k_x k_y \sigma_y \}, \end{aligned} \quad (2)$$

where σ_i are the Pauli matrices (σ_0 is the unity matrix), $\mathbf{k} = (k_x, k_y)$ are the electron momentum components, $\tau = \pm 1$ is the valley index, $s = \pm 1$ denotes charge

	a	d	ϵ	Δ_0	m	λ_c	λ_v
MoS ₂	3.185	6.12	16.3	2.087	0.520	-1.41	74.60
MoSe ₂	3.319	6.54	17.9	1.817	0.608	-10.45	93.25
WS ₂	3.180	6.14	14.6	2.250	0.351	15.72	213.46
WSe ₂	3.319	6.52	16.0	1.979	0.379	19.85	233.07

TABLE I. Model parameters for TMDC monolayers. Lattice constants a (Å), effective masses m , and spin-orbit coupling constants $\lambda_{c,v}$ (meV) are taken from Ref. [60], monolayer thicknesses d (Å) and static dielectric constants ϵ are from Ref. [61], and Δ_0 (eV) is from Ref. [62].

carrier spin, v_F is the Fermi velocity, Δ is the gap between the conduction and the valence bands, and $\lambda_{c,v}$ are the spin splittings of the conduction c and valence v bands. The Fermi velocity is given as $\hbar v_F = \sqrt{\Delta/2m}$ [50], and the trigonal warping constant is determined as $\kappa = -\sqrt{3}/24\hbar v_F a$ [56, 58]. Finally, we assume the following model to describe the dependence of the bandgap on the dielectric environment [59]

$$\begin{aligned} \Delta = \Delta_0 + \frac{e^2}{2\epsilon d} \left[\frac{L_2 + L_1}{\sqrt{L_2 L_1}} \operatorname{tanh}^{-1}(\sqrt{L_2 L_1}) \right. \\ \left. - \ln(1 - L_2 L_1) \right], \quad L_i = \frac{\epsilon - \epsilon_i}{\epsilon + \epsilon_i}, \end{aligned} \quad (3)$$

where ϵ is the bulk dielectric constant of the TMDC material, Δ_0 is its bulk bandgap, $\epsilon_{i=1,2}$ are dielectric constants of the lower and upper dielectric environment, and d is the monolayer thickness. Eigenstates of the Dirac Hamiltonian are classified as quasi-electrons $|c\mathbf{k}\rangle$ with energies $\varepsilon_{c\mathbf{k}}$ above the gap and quasi-holes $|v\mathbf{k}\rangle$ with energies $\varepsilon_{v\mathbf{k}}$ below the gap. Indices c and v denote all state quantum numbers except for the quasimomentum \mathbf{k} . Monolayers of semiconductors MoS₂, MoSe₂, WS₂, and WSe₂ have a similar crystal configuration and qualitatively similar energy dispersion of the lowest energy single-particle states. The effective Dirac model parameters for those materials are obtained by fitting results of the first-principle band structure calculations and are summarized in Table I.

With additional contributions due to the trigonal warping, the minimal coupling model describes the interaction between quasiparticles and the driving electromagnetic field. We use a common assumption that the external field has a very large wavelength compare to other system characteristic sizes. Using this assumption, we obtain the following interaction Hamiltonian for the states of momentum \mathbf{k} :

$$H_f(\mathbf{k}) = -\frac{e}{c\hbar} \sum_{\alpha} p_{\mathbf{k}}^{\alpha} A_{\alpha} + \frac{e^2}{2c^2\hbar^2} \sum_{\alpha\beta} q_{\mathbf{k}}^{\alpha\beta} A_{\alpha} A_{\beta}, \quad (4)$$

where \mathbf{A} is the field vector potential, and coefficients of the linear and quadratic interaction terms are obtained

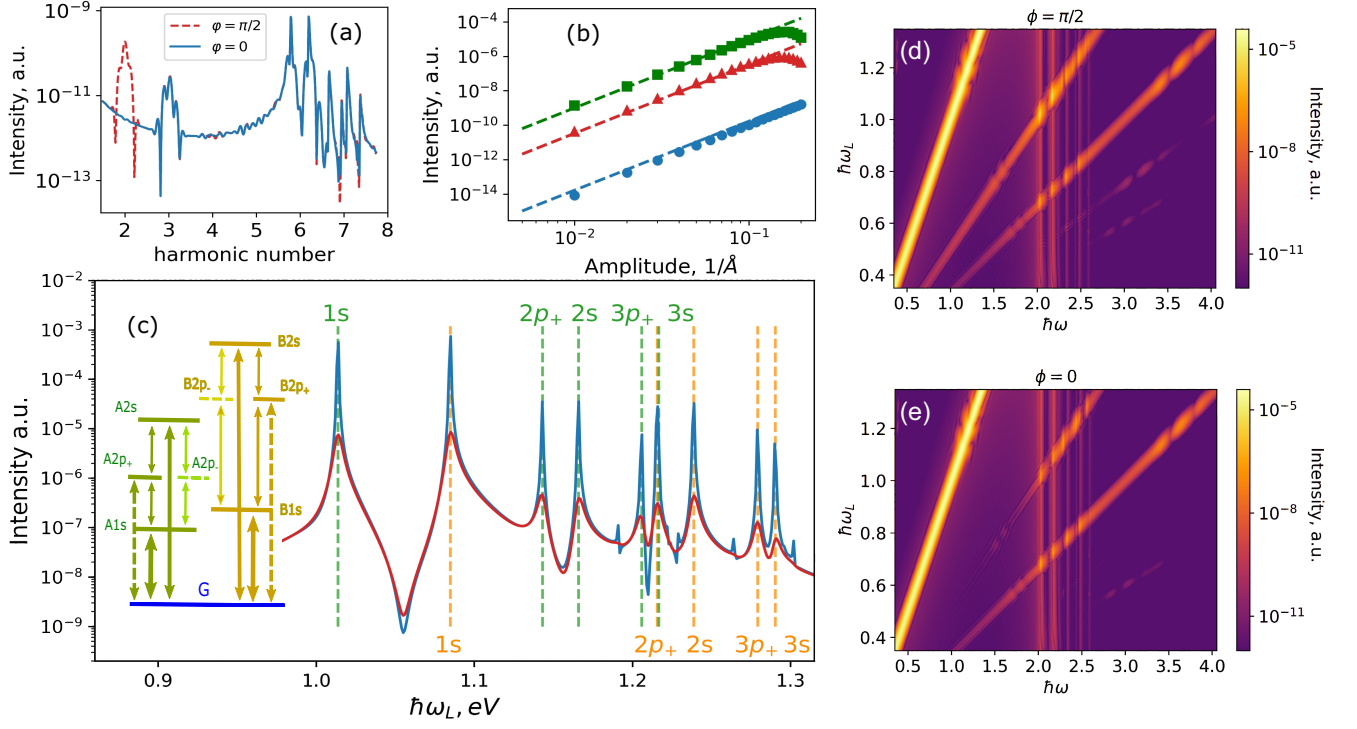


FIG. 1. (a) Spectral intensity of the nonlinear response $I_{\omega_L, \omega}$ calculated at $f = 0.5 \text{ \AA}^{-1}$ and $\hbar\omega_L = 0.35 \text{ eV}$ (off-resonance) for polarization angle $\phi = 0$ (blue) and $\phi = \pi/2$ (red). (b) SHG intensity $I_{\omega_L, 2\omega_L}$ calculated for the off-resonant driving with $\hbar\omega_L = 0.35 \text{ eV}$ (blue circles), in resonance with $A1s$ exciton (green squares), and in resonance with $A2p_+$ exciton state (red triangles). Dashed lines show the perturbation theory result $I \propto f^4$. (c) SHG intensity as a function of $\hbar\omega_L$ calculated at $f = 0.1 \text{ \AA}^{-1}$ without dephasing ($\gamma = 0$, blue line) and with dephasing ($\gamma = 10 \text{ meV}$, red line). A and B excitons are marked by green and orange dashed lines. The inset is a schematic energy diagram (not to scale) of optically active low-energy excitons in a MoS_2 monolayer. Solid arrows mark transitions allowed in a rotationally invariant system; dashed lines are warping mediated transitions. (d-e) Color density high harmonic intensity spectrum as a function of the driving frequency $I_{\omega_L, \omega}$ calculated for two polarization angles $\phi = \pi/2$ and 0 , respectively.

as derivatives:

$$p_{\mathbf{k}}^\alpha = \frac{\partial H_0(\mathbf{k})}{\partial k_\alpha}, \quad q_{\mathbf{k}}^{\alpha\beta} = \frac{\partial^2 H_0(\mathbf{k})}{\partial k_\alpha \partial k_\beta}. \quad (5)$$

Notice that unlike the Schrodinger equation with the quadratic dispersion, the term with the second power of the field facilitates transitions between single-particle states and thus cannot be neglected.

B. Exciton states

The full many-body Hamiltonian with the Coulomb interaction between electrons and holes is projected onto a basis of two-particle states $|cv\rangle = c_{c\mathbf{k}}^\dagger d_{v\mathbf{k}}^\dagger |0\rangle$. Using the basis of these states, excitons are obtained by solving the Bethe – Salpeter equation (BSE) [63] that takes into account screening due to the environment that embeds the monolayer [48, 49]. Solving the BSE is equivalent to finding eigenstates of the effective two-particle Hamiltonian

H_{ex} defined by its matrix elements as

$$\langle c'v' | H_{ex} | cv \rangle = (\varepsilon_c - \varepsilon_v) \delta_c^c \delta_v^v - W_{v'c'}^{vc} + V_{v'c'}^{c'v}, \quad (6)$$

where $\varepsilon_{ck, vk}$ are single-particle energies, and W and V are the screened and bare Coulomb potentials. The latter is defined as $V_{cd}^{ab} = V(\mathbf{k}_a - \mathbf{k}_c) \langle u_c | u_a \rangle \langle u_d | u_b \rangle$, with $\langle u_c | u_a \rangle$ being the overlap of the single-particle Bloch states, and $V(\mathbf{q}) = 2\pi e^2 / q$. In Eq. (6), momentum index \mathbf{k} is absorbed in indexes c and v for brevity. In the screened potential one changes $V(\mathbf{q})$ for

$$W(\mathbf{q}) = \frac{2\pi e^2}{q} \begin{cases} \varepsilon_{env}^{-1} (1 + r_0 q)^{-1}, & q \in \text{intra-valley}; \\ \varepsilon^{-1}, & q \in \text{inter-valley}, \end{cases} \quad (7)$$

so that the intravalley screening (small q) is described by the Rytova-Keldysh potential [64, 65] whereas the inter-valley screening is reduced to the bulk dielectric constant ε [50]. Here $\varepsilon_{env} = (\varepsilon_1 + \varepsilon_2) / 2$ is determined by the dielectric environment, and the screening length is $r_0 = \varepsilon d / 2$. We present results for $\varepsilon_{env} = 1$ throughout the paper,

unless otherwise stated.

The large wavelength assumption for the driving field implies that the excitation does not change the total momentum, and thus only zero-momentum particle-hole pairs contribute to exciton states

$$|\Psi_a\rangle = \sum_{\mathbf{k}} \sum_{cv} X_{\mathbf{k}cv}^a c_{\mathbf{k}c}^\dagger d_{\mathbf{k}v}^\dagger |0\rangle, \quad (8)$$

where $X_{\mathbf{k}cv}^a$ are eigenvectors of the Hamiltonian (6). In the numerical calculations, we use a mesh of $480 \times 480 \times 1$ in the Brillouin zone. The momentum cut-off k_c is introduced to restrict the number of single-particle states near the K and K' valleys. A chosen value of $k_c = 0.4 \text{ \AA}^{-1}$ is sufficient for numerical convergence.

The interaction Hamiltonian in the exciton states representation is found as

$$H_f = -\frac{e}{\hbar} \sum_{\alpha} P_{\alpha} A_{\alpha} + \frac{e^2}{2c^2 \hbar^2} \sum_{\alpha\beta} Q^{\alpha\beta} A_{\alpha} A_{\beta}, \quad (9)$$

where operators P_{α} and $Q_{\alpha\beta}$ are obtained by calculating field-induced matrix elements of the interaction Hamiltonian (4) for transitions between exciton eigenstates in Eq. (8). For transitions that involve the ground state without exciton (index $b = 0$) one obtains the matrix elements as

$$\begin{aligned} P_{a0}^{\alpha} &= \frac{1}{N} \sum_{\mathbf{k}} \sum_{cv} p_{\mathbf{k}cv}^{\alpha} X_{\mathbf{k}cv}^{a*}, \\ Q_{a0}^{\alpha\beta} &= \frac{1}{N} \sum_{\mathbf{k}} \sum_{cv} q_{\mathbf{k}cv}^{\alpha\beta} X_{\mathbf{k}cv}^{a*}, \end{aligned} \quad (10)$$

where N is the number of the \mathbf{k} -mesh points, while for transitions between different exciton states (of the same total momentum), one gets

$$\begin{aligned} P_{ab}^{\alpha} &= \sum_{\mathbf{k}} \sum_{cc'vv'} X_{\mathbf{k}cv}^{a*} (p_{\mathbf{k}cc'}^{\alpha} \delta_v^{v'} - p_{\mathbf{k}vv'}^{\alpha} \delta_c^{c'}) X_{\mathbf{k}c'v'}^b, \\ Q_{ab}^{\alpha\beta} &= \sum_{\mathbf{k}} \sum_{cc'vv'} X_{\mathbf{k}cv}^{a*} (q_{\mathbf{k}cc'}^{\alpha\beta} \delta_v^{v'} - q_{\mathbf{k}vv'}^{\alpha\beta} \delta_c^{c'}) X_{\mathbf{k}c'v'}^b. \end{aligned}$$

The single-particle transition matrix elements in these expressions are given as

$$p_{\mathbf{k}rr'}^{\alpha} = \langle r | p_{\mathbf{k}}^{\alpha} | r' \rangle, \quad q_{\mathbf{k}rr'}^{\alpha\beta} = \langle r | q_{\mathbf{k}}^{\alpha\beta} | r' \rangle, \quad (11)$$

where r denotes c or v states. In the numerical calculations, we use 48 lowest energy excitonic states (twelve four-fold degenerate states), which is sufficient for the numerical convergence of the results.

C. Nonlinear dynamics and harmonics generation

The dynamics is obtained by solving the LvN equation (1) with the driving pulse. The vector potential of the driving field is assumed tangential to the

TMDC monolayer with the spatial components $\mathbf{A}(t) = A(t)(\cos(\phi), \sin(\phi), 0)$, where angle ϕ is measured from the zig-zag axis of the monolayer TMDC. The time dependence is monochromatic with the frequency ω_L and Gaussian envelope function

$$A(t) = \frac{c\hbar f}{e} \cos(\omega_L t) e^{-(t-t_0)^2/2\sigma^2}, \quad (12)$$

with typical pulse parameters [16] of $t_0 = 80$ fs, $\sigma = 25$ fs, and pulse duration 150 fs. The electric field amplitude is found from the vector potential in the usual way. When the envelope function varies slowly in comparison with the oscillation period, the field strength is approximately $\mathbf{E} \approx \mathbf{A}\omega_L/c$, which is related to the driving amplitude f as $E = \hbar\omega_L f/e$.

To account for losses and corresponding finite exciton lifetime, we consider the pure dephasing mechanism without transitions. It is described by diagonal Lindblad operators $\Gamma_a = |a\rangle\langle a|$ in the basis of excitonic states $|a\rangle$. For simplicity, we also assume an equal dephasing rate $\gamma_a = 10$ meV for all excitons. We note that our conclusions do not depend qualitatively on the details of the loss mechanism. The LvN Eq. (1) is solved using Quantum Toolbox in Python (QuTiP) [66, 67]. The obtained solution for the density matrix is then used to calculate the time evolution of the polarization operator by taking the trace

$$\bar{P}^{\alpha}(t) = \text{Tr}[\rho P^{\alpha}]. \quad (13)$$

The second and higher harmonics are extracted separately from the Fourier components of \bar{P}^{α} . In the calculations, we use the maximal propagation time of $t_{max} = 2.5$ ps to ensure that the steady-state is achieved. Polarization components are very sensitive to the polarization angle ϕ of the excitation pulse. When the emitted light is detected at the same polarization angle, which is a common experimental setup [9–11, 16, 22, 32], the spectral intensity of the detected signal is proportional to

$$I_{\omega_L, \omega} \propto |\bar{P}_{\omega_L, \omega}^x \cos(\phi) + \bar{P}_{\omega_L, \omega}^y \sin(\phi)|^2. \quad (14)$$

The intensities of second and higher harmonics are given by $I_n = I_{\omega_L, n\omega_L}$, where n is an integer.

III. NUMERICAL RESULTS

A. Exciton-mediated nonlinear spectrum

A typical nonlinear spectrum of a standalone MoS₂ monolayer in Fig. 1a is calculated for the off-resonant excitation with the frequency $\hbar\omega_L = 0.35$ eV far below the lowest exciton state with energy $\varepsilon = 2.03$ eV. The largest excitation field strength $E = 0.175$ V/Å in Fig. 1 corresponds to the driving amplitude of $f = 0.5 \text{ \AA}^{-1}$.

Figure 1a reveals clearly second ($n = 2$) and third ($n = 3$) harmonics below the lowest excitonic resonance of $n \approx$

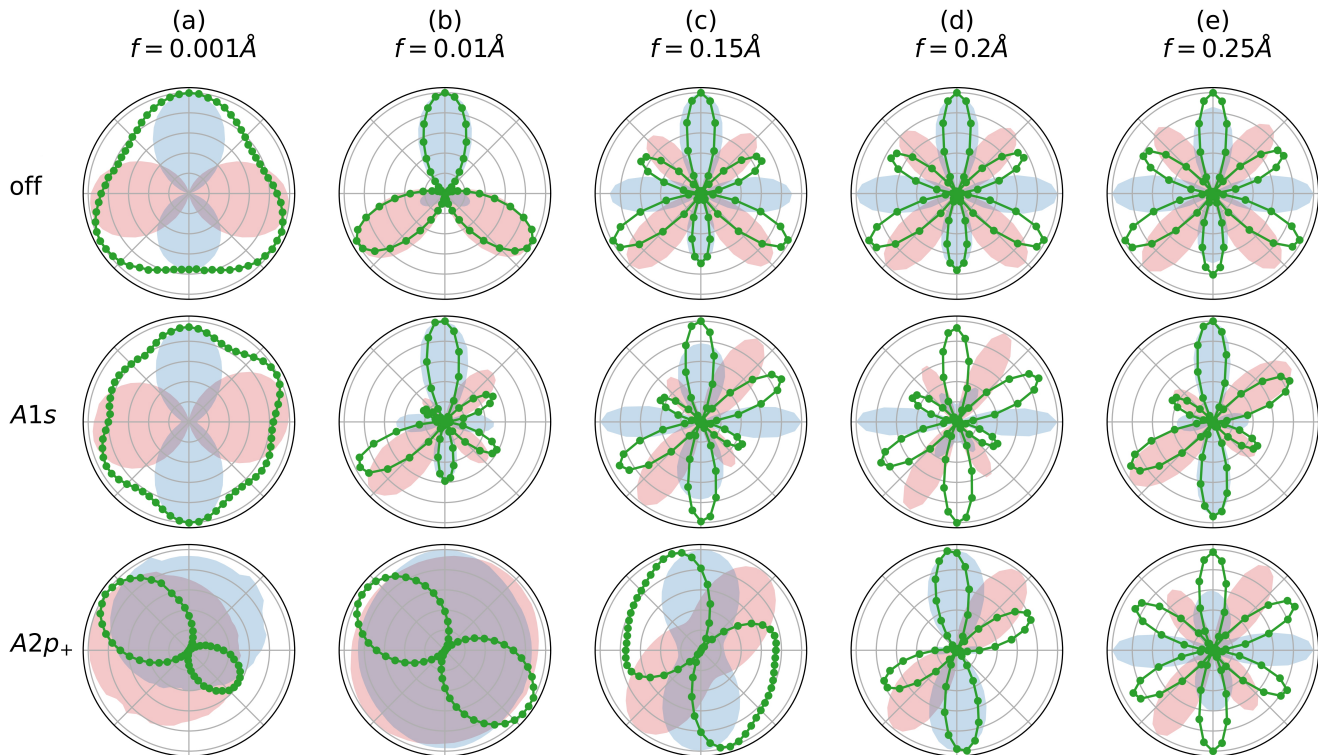


FIG. 2. Polarization angle dependence of SHG intensity (green points) and polarization components $|\bar{P}^x|$ (red shading) and $|\bar{P}^y|$ (blue shading) calculated at $f = 10^{-3} \text{ \AA}^{-1}$ (a), $f = 10^{-2} \text{ \AA}^{-1}$ (b), $f = 0.15 \text{ \AA}^{-1}$ (c), $f = 0.2 \text{ \AA}^{-1}$ (d), and $f = 0.25 \text{ \AA}^{-1}$ (e). Upper row: off-resonant excitation with $\hbar\omega_L = 0.35 \text{ eV}$; middle row: $\hbar\omega_L = 1.015 \text{ eV}$ is in resonance with the energy of $A1s$ exciton; lowest row: $\hbar\omega_L = 1.14 \text{ eV}$ is in resonance with the $A2p_+$ exciton. The results are normalized to their maximal values.

6. The SHG signal is very sensitive to the polarization angle, completely vanishing at $\phi = 0$. At higher ω , the spectrum is practically independent of the angle. When the driving amplitude is small, the dependence of the SHG intensity on the driving amplitude, shown in Fig. 1b, follows a standard result $I_2 \propto f^4$ of the perturbation theory, which breaks down when $f \gtrsim 0.2 \text{ \AA}^{-1}$.

The SHG intensity dependence on the driving frequency in Fig. 1c reveals sharp peaks when $2\hbar\omega_L$ coincides with exciton energy (resonance). There are different types of excitonic states that are classified like atomic orbitals (s, p, \dots) with the extra complexity introduced by the valley and spin degrees of freedom. The amplitude of the resonance peaks is very sensitive to the loss rate γ which is clearly seen when comparing the peak amplitudes with and without the loss. Away from resonances, the signal is insensitive to the loss rate.

Further characteristics of the nonlinear response are demonstrated in Figs. 1d and 1e, which show color density plots of the spectral intensity $I_{\omega_L, \omega}$ depending on both ω_L and ω . The calculations are done for $f = 0.1 \text{ \AA}^{-1}$ and two polarization angles $\phi = \pi/2$ and 0 . The results confirm that the second harmonic is absent at $\phi = 0$ for the off-resonant excitation [cf. Fig. 1a]. However, one sees that the SHG becomes visible even at $\phi = 0$ when the

driving frequency reaches the first excitonic resonance of $2\hbar\omega_L \simeq 2\text{eV}$. This indicates a non-trivial dependence on the polarization angle we now explore in detail.

B. Polarization diagrams

The SHG dependence on the polarization angle is illustrated in Fig. 2, which plots the angular dependence of $I_2(\phi)$: here, the value of I_2 is given by the radial distance from the diagram center. The resulting polarization diagrams, shown in Fig. 2, are calculated for a standalone MoS_2 monolayer for selected values of f and three frequencies ω_L , chosen to represent off-resonant excitation, the excitation at resonance with $A1s$ and $A2p_+$ states [see Fig. 1c]. SHG intensity I_2 defined by Eq. (14) depends on polarization components, $|\bar{P}^x|$ and $|\bar{P}^y|$, that are also shown in Fig. 2 by the color shading, for comparison. It is clearly seen that polarization diagrams are very sensitive to both the amplitude f and frequency ω_L of the driving field.

In the linear response limit of $f \rightarrow 0$, the polarization diagram is circular in all cases (not shown). At the same time, at the very strong driving, it reveals a familiar symmetric six-leaf pattern. This pattern is defined by the

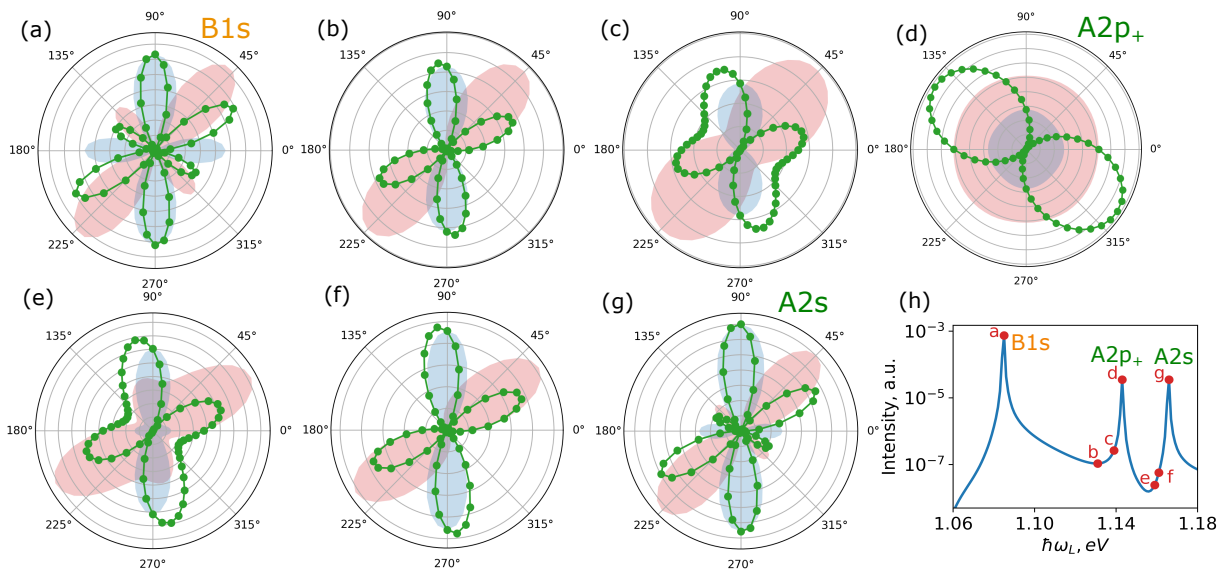


FIG. 3. Angular dependence of I and $|P_{x,y}|^2$ for the SHG in MoS₂ monolayer (a)-(g), calculated for driving field energies $\hbar\omega_L$ marked by the red points in the panel (h) [cf. Fig. 1c]. The driving amplitude is $f = 0.1 \text{ \AA}^{-1}$.

single-particle dynamics that follows the crystal symmetry of MoS₂, and can be used to establish the orientation of the crystal lattice in experiments [9–13, 32]. Excitonic states start to play a much more significant role in the dynamics for the weaker driving. This is accompanied by drastic changes in the polarization diagram.

When the excitation is off-resonant and f increases, the polarization diagram first develops a triangular shape, symmetric with respect to 120° rotations. With the further increase in f , the angular dependence becomes, consecutively, first a three-leaf and then a six-leaf pattern. At still larger f , the six-leaf pattern becomes symmetric. Changes in the angular dependence of I_2 are accompanied by those in components P^x and P^y , also shown in Fig. 2.

When the driving frequency is at resonance with an exciton state, the polarization diagram changes qualitatively depending on the exciton type. In the $A1s$ exciton resonance, the diagram develops an asymmetric six-leaf pattern already at very small amplitudes. The same six-leaf pattern remains for all values of f becoming more symmetric at stronger driving.

In contrast, in the $A2p_+$ exciton resonance in Fig. 2, a six-leaf pattern is seen only at $f = 0.25 \text{ \AA}^{-1}$, while at weaker driving, the diagram differs from both the off-resonant and the $A1s$ resonance cases. For a weaker driving with $f = 10^{-3} \text{ \AA}^{-1}$, the angular dependence has an asymmetric two-leaf shape. It becomes fully symmetric at larger amplitude $f = 10^{-2} \text{ \AA}^{-1}$. When f increases, the butterfly-like pattern is formed with two equal side wings. With a further decrease in f , one observes four- and, then, six-leaf shapes.

Exciton-dependent differences in the polarization diagrams are further explored by tracing how the angular dependence changes with frequency ω_L . Figure 3 illus-

trates the changes by showing a diagram sequence calculated for values of ω_L in the interval between $B1s$ and $A2s$ states (the calculations are done at $f = 0.1 \text{ \AA}^{-1}$). When ω_L increases, a non-symmetric six-leaf shape, observed at the $B1s$ resonance, first changes to a four-leaf pattern, then develops a butterfly-like shape with two wings, before transforming itself into a two-leaf pattern at the $A2p_+$ resonance. With a further increase of ω_L , these transformations take place in the reversed order, producing the original asymmetric six-leaf pattern when the $A2s$ resonance is reached.

One notes the polarization diagrams observed at $A1s$, $B1s$ and $A2s$ resonances, shown in Figs. 2 and 3, have only marginal quantitative differences. This indicates the SHG angular dependence is similar for excitonic states of the same spatial configuration. The angular dependence at different resonances is distinguishable only when excitons have different configurations. Figures 2 and 3 give one notable example of this type: the angular dependence observed at the $A2p_+$ resonance deviates strongly from the $A1s$, $B1s$, and $A2s$ resonances. The same applies to the polarization components $P^{x,y}$ [see Fig. 3] implying this conclusion holds for arbitrary measurements setup for SHG polarization.

C. Comparing different materials

We now compare SHG polarization diagrams for monolayers of MoS₂, MoSe₂, WS₂, and WSe₂. These materials have a qualitatively similar crystal configuration and, therefore, a similar band structure. One also identifies the same types of excitonic states, i.e. s, p , although their spectral positions differ. When the same states are identified, one calculates corresponding SHG polarization

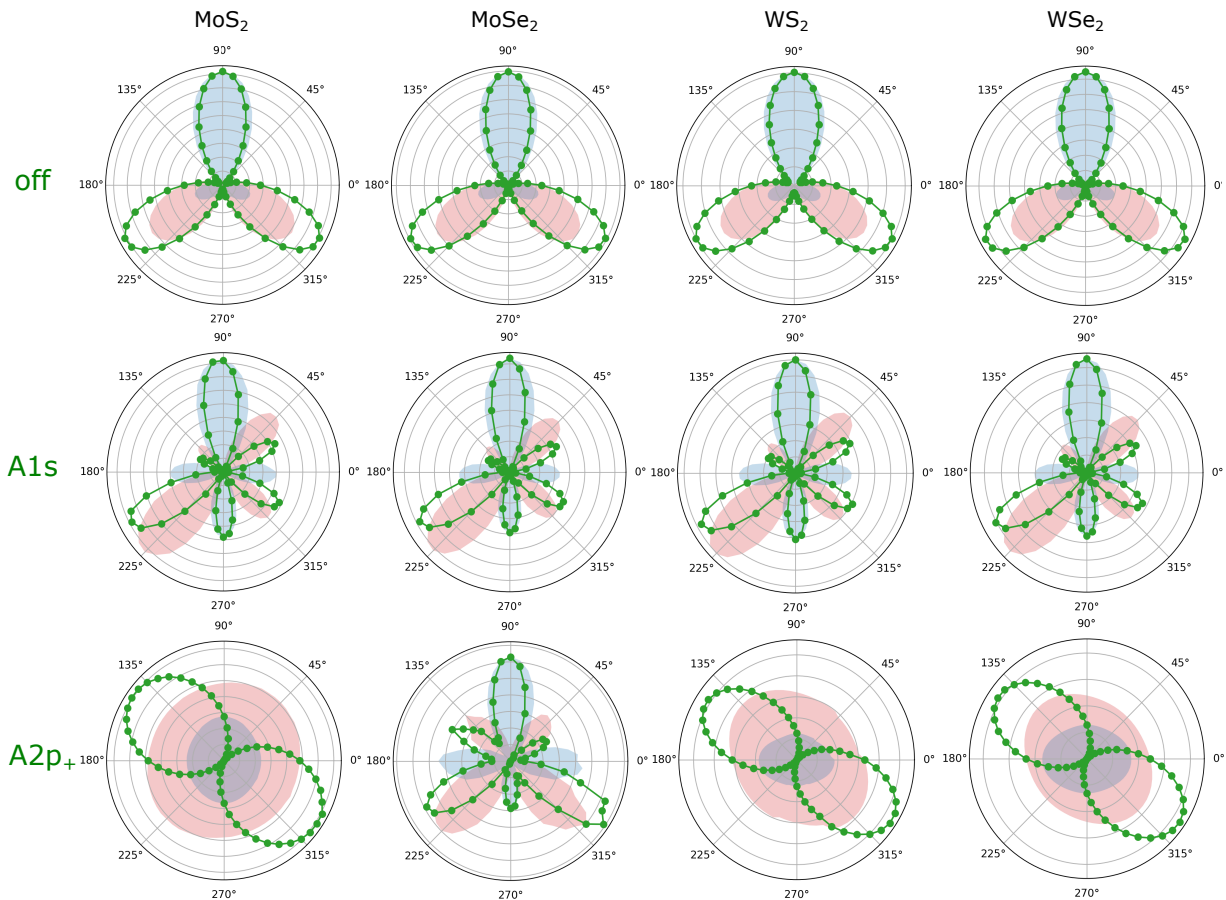


FIG. 4. Angular dependence of the SHG intensity (green points) and polarization components $|P_x|^2$ (red shading) and $|P_y|^2$ (blue shading) for the driving amplitude $f = 0.1 \text{ \AA}^{-1}$, calculated for monolayers MoS₂, MoSe₂, WS₂, and WSe₂ (panel columns) for the off-resonant driving with $\hbar\omega_L = 0.35\text{eV}$ (upper row), at resonance with the $A1s$ state (middle row), and at resonance with the $A2p_+$ state (lower row).

diagrams.

Results in Fig. 4 plots the diagrams for these four materials calculated for the off-resonant driving, and the $A1s$ and $A2p_+$ resonances. One sees the angular dependencies are indeed similar for all materials except for the $A2p_+$ resonance where MoSe₂ differs notably. The difference is explained by the fact that energies of $A2p_+$ and $B1s$ states almost coincide in MoSe₂. This near degeneracy results in a mixture of signals typical for $B1s$ and $A2p_+$ resonances, which both contribute to the SHG and distort the angular dependence.

IV. DISCUSSION

A big variety of observed SHG polarization diagram types originate in the interplay of several factors affecting single- and two-particle states. Crystal symmetry is one of the factors defining SHG angular dependence. It is taken into account by the tri-diagonal warping in the Dirac model for single-particle states. The warping violates the rotational symmetry, allowing additional op-

tical transitions. This is illustrated in the inset in Fig. 1c that shows a schematic structure of the low energy exciton states contributing most to the nonlinear dynamics. A rotational symmetry admits transitions illustrated in this scheme by solid arrows. Optical transitions cannot connect any three-state sequence making SHG forbidden in a rotationally invariant system, which can be formally shown, e.g., by solving the LvN equation perturbatively. The tri-diagonal warping breaks the rotational symmetry allowing transitions between the states G and $2p_+$ (see Fig. 1). This creates four three-state sequences, $G \rightarrow 1s \rightarrow 2p_+$ and $G \rightarrow 2s \rightarrow 2p_+$, for A and B states, respectively, giving rise to SHG.

Another source of SHG is the quadratic term in the field-matter interaction Hamiltonian H_f , also introduced by the warping. The crystal symmetry is reflected in the matrix elements of P^α and $Q^{\alpha\beta}$ dipole operators entering H_f . There is a particular relation between these matrix elements and the SHG angular dependence, which can be illustrated by estimating the polarization vector components in H_f . Assuming symmetric transition matrix

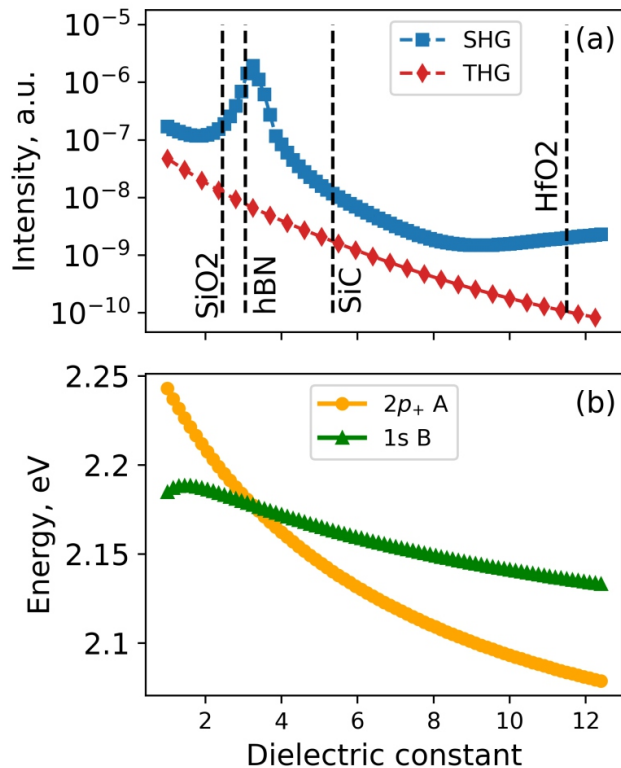


FIG. 5. (a) Intensity of the second (blue circles) and third (red triangles) harmonics on MoS₂ for the driving amplitude $f = 0.1\text{\AA}^{-1}$ at resonance with the $A2p_+$ state as a function of the environment dielectric constant $\epsilon_{env} = (\epsilon_1 + 1)/2$, where ϵ_1 is the static dielectric constant of the substrate. The dashed vertical lines correspond to ϵ_{env} values for the most commonly used substrates. (b) Energy of $B1s$ (red triangles) and $A2p_+$ excitons (blue circles) as a function of the environment dielectric constant.

elements, one obtains a simple expression

$$\begin{aligned} P_x(\phi) &= \tilde{f} \cos(\phi) - \alpha \tilde{f}^2 \sin(2\phi), \\ P_y(\phi) &= \tilde{f} \sin(\phi) - \alpha \tilde{f}^2 \cos(2\phi), \end{aligned} \quad (15)$$

where $\tilde{f} \propto f$. By substituting this polarization vector into Eq. (14) and assuming α is a fitting parameter, one can quantitatively reproduce all the SHG angular dependencies for the off-resonant case in Fig. 2. When \tilde{f} is small, the polarization is determined by the linear contribution, such that the SHG intensity is independent of the angle. In contrast, the larger driving field activates the quadratic contribution, which dominates the angular dependency of $I(\phi)$. In this case, a symmetric six-leaf pattern emerges, as shown in Fig. 2. In the regime of intermediate driving amplitude, the contributions of the linear and quadratic terms are comparable, and one observes a crossover between these two extreme regimes.

However, Eq. (15) can be used only for the case of the off-resonant excitation. At resonance with an exci-

tonic state, the angular dependence becomes more complex due to a strong influence of the two-particle interactions. Configuration of an exciton state enables specific transition matrix elements, and this distorts the symmetry of the SHG angular dependence, as shown in Fig. 2 for $A1s$ and $A2p_+$ resonances. In addition, the Coulomb interaction enhances the dipole transitions and, hence, the linear term in Eq. (9).

Our results show that changes induced by the exciton-related effects are most notable at the $2p_+$ -states resonances, where the linear term in Eq. (9) is dominant in a large interval of f values. The crossover between the regimes of mostly linear and mostly quadratic contributions in the light-matter interaction H_f takes place at $f_c \simeq 0.2\text{\AA}^{-1}$. This coincides with the upper applicability limit for the perturbation theory result $I \propto f^4$ in Fig. 1b. The stronger the driving, the larger is the quadratic contribution, and thus closer to the symmetric six-leaf polarization diagram.

Finally, we discuss the influence of the dielectric environment on the excitonic effects in the nonlinear response. The environment affects the effective dielectric constant of the system, modifying the strength of the Coulomb interaction, the binding energy of excitons, and, thus, their contribution to the dynamics. This is illustrated in Fig. 5a, which plots the intensity of the second and third harmonics at resonance with the $A2p_+$ state as functions of the environment dielectric constant ϵ_{env} . As ϵ_{env} increases from 1 to 10, the intensity of both harmonics decreases by more than two orders of magnitude. A sharp peak in the SHG signal at $\epsilon_{env} \simeq 4$ in Fig. 5a appears due to the degeneracy of the $A2p_+$ and $B1s$ energies at this point [see Fig. 5b].

V. CONCLUSIONS

Our work demonstrates that SHG in TMDC monolayers is notably affected by the many-particle exciton effects. The SHG signal increases by orders of magnitude when the driving pulse is at resonance with an excitonic state. More importantly, excitons alter the SHG polarization angular dependence qualitatively. Its dependence on the energy and amplitude of the driving field undergoes significant changes depending on the type of the resonating exciton. The influence of excitons gives rise to deviations from the symmetric six-leaf angular dependence in monolayers with an undistorted crystal structure. This conclusion is generic, being supported by the qualitatively similar polarization patterns and their changes obtained for MoS₂, MoSe₂, WS₂, and WSe₂. Our results open a pathway to a nonlinear spectroscopy method to probe exciton states by the symmetry of the polarization angular dependence of the SHG signal measured as a function of the excitation strength.

ACKNOWLEDGMENTS

We acknowledge support by the Russian Science Foundation under the grant 18-12-00429 used for numerical calculations. A. V. K., V. D. N., and A. E. L. thank the Ministry of Science and Higher Education of the Russian Federation (state assignment project No. 0723-2020-

0036) and NRNU MEPhI high-performance computing center. Y. V. Z. is grateful to the Deutsche Forschungsgemeinschaft (DFG, German Research Foundation) SPP 2244 (Project-ID 443416183) for the financial support. V. P. gratefully acknowledges Tony Heinz for informative and stimulating discussions, funding from the Vice President for Research and Economic Development (VPRED) and SUNY Research Seed Grant Program, and computational facilities at the Center for Computational Research at the University at Buffalo (<http://hdl.handle.net/10477/79221>).

-
- [1] R. W. Boyd, *Nonlinear Optics* (Academic Press, New York, USA, 2020).
- [2] S. Ghimire, A. D. DiChiara, E. Sistrunk, P. Agostini, L. F. DiMauro, and D. A. Reis, *Observation of high-order harmonic generation in a bulk crystal*, *Nature Physics* **7**, 138 (2010).
- [3] A. H. Chin, O. G. Calderón, and J. Kono, *Extreme mid-infrared nonlinear optics in semiconductors*, *Physical Review Letters* **86**, 3292 (2001).
- [4] A. Belyanin, F. Xie, D. Liu, F. Capasso, and M. Troccoli, *Coherent nonlinear optics with quantum cascade structures*, *Journal of Modern Optics* **52**, 2293 (2005).
- [5] P. N. Prasad and D. J. Williams, *Introduction to Nonlinear Optical Effects in Molecules and Polymers* (Wiley-Interscience, New York, USA, 1991).
- [6] L. D. Dominicis, S. Botti, L. S. Asilyan, R. Ciardi, R. Fantoni, M. L. Terranova, A. Fiori, S. Orlanducci, and R. Appolloni, *Second- and third-harmonic generation in single-walled carbon nanotubes at nanosecond time scale*, *Applied Physics Letters* **85**, 1418 (2004).
- [7] Y. Murakami and J. Kono, *Nonlinear photoluminescence excitation spectroscopy of carbon nanotubes: Exploring the upper density limit of one-dimensional excitons*, *Physical Review Letters* **102**, 037401 (2009).
- [8] J. Kono, *Ultrafast and nonlinear optics in carbon nanomaterials*, *Journal of Physics: Condensed Matter* **25**, 050301 (2013).
- [9] N. Kumar, S. Najmaei, Q. Cui, F. Ceballos, P. M. Ajayan, J. Lou, and H. Zhao, *Second harmonic microscopy of monolayer MoS₂*, *Physical Review B* **87**, 161403 (2013).
- [10] L. M. Malard, T. V. Alencar, A. P. M. Barboza, K. F. Mak, and A. M. de Paula, *Observation of intense second harmonic generation from MoS₂ atomic crystals*, *Physical Review B* **87**, 201401 (2013).
- [11] X. Yin, Z. Ye, D. A. Chenet, Y. Ye, K. O'Brien, J. C. Hone, and X. Zhang, *Edge nonlinear optics on a MoS₂ atomic monolayer*, *Science* **344**, 488 (2014).
- [12] D. J. Clark, V. Senthilkumar, C. T. Le, D. L. Weerawarne, B. Shim, J. I. Jang, J. H. Shim, J. Cho, Y. Sim, M.-J. Seong, S. H. Rhim, A. J. Freeman, K.-H. Chung, and Y. S. Kim, *Strong optical nonlinearity of CVD-grown MoS₂ monolayer as probed by wavelength-dependent second-harmonic generation*, *Physical Review B* **90**, 121409 (2014).
- [13] W.-T. Hsu, Z.-A. Zhao, L.-J. Li, C.-H. Chen, M.-H. Chiu, P.-S. Chang, Y.-C. Chou, and W.-H. Chang, *Second harmonic generation from artificially stacked transition metal dichalcogenide twisted bilayers*, *ACS Nano* **8**, 2951 (2014).
- [14] C. Janisch, Y. Wang, D. Ma, N. Mehta, A. L. Elías, N. Perea-López, M. Terrones, V. Crespi, and Z. Liu, *Extraordinary second harmonic generation in tungsten disulfide monolayers*, *Scientific Reports* **4**, 5530 (2014).
- [15] T. Jiang, H. Liu, D. Huang, S. Zhang, Y. Li, X. Gong, Y.-R. Shen, W.-T. Liu, and S. Wu, *Valley and band structure engineering of folded MoS₂ bilayers*, *Nature Nanotechnology* **9**, 825 (2014).
- [16] H. Liu, Y. Li, Y. S. You, S. Ghimire, T. F. Heinz, and D. A. Reis, *High-harmonic generation from an atomically thin semiconductor*, *Nature Physics* **13**, 262 (2016).
- [17] A. Säynäjoki, L. Karvonen, H. Rostami, A. Autere, S. Mehravar, A. Lombardo, R. A. Norwood, T. Hasan, N. Peyghambarian, H. Lipsanen, K. Kieu, A. C. Ferrari, M. Polini, and Z. Sun, *Ultra-strong nonlinear optical processes and trigonal warping in MoS₂ layers*, *Nature Communications* **8**, 893 (2017).
- [18] A. Autere, H. Jussila, Y. Dai, Y. Wang, H. Lipsanen, and Z. Sun, *Nonlinear optics with 2d layered materials*, *Advanced Materials* **30**, 1705963 (2018).
- [19] L. Mennel, M. M. Furchi, S. Wachter, M. Paur, D. K. Polyushkin, and T. Mueller, *Optical imaging of strain in two-dimensional crystals*, *Nature Communications* **9**, 516 (2018).
- [20] L. Mennel, M. Paur, and T. Mueller, *Second harmonic generation in strained transition metal dichalcogenide monolayers: MoS₂, MoSe₂, WS₂, and WSe₂*, *APL Photonics* **4**, 034404 (2019).
- [21] T. Stiehm, R. Schneider, J. Kern, I. Niehues, S. M. de Vasconcelos, and R. Bratschitsch, *Supercontinuum second harmonic generation spectroscopy of atomically thin semiconductors*, *Review of Scientific Instruments* **90**, 083102 (2019).
- [22] G. M. Maragkakis, S. Psilodimitrakopoulos, L. Mouchliadis, I. Paradisanos, A. Lemonis, G. Kioseoglou, E. Stratakis, and and, *Imaging the crystal orientation of 2d transition metal dichalcogenides using polarization-resolved second-harmonic generation*, *Opto-Electronic Advances* **2**, 19002601 (2019).
- [23] K.-Q. Lin, S. Bange, and J. M. Lupton, *Quantum interference in second-harmonic generation from monolayer WSe₂*, *Nature Physics* **15**, 242 (2019).
- [24] J. Zhang, W. Zhao, P. Yu, G. Yang, and Z. Liu, *Second harmonic generation in 2d layered materials*, *2D Materials* **7**, 042002 (2020).

- [25] A. R. Khan, B. Liu, T. Lü, L. Zhang, A. Sharma, Y. Zhu, W. Ma, and Y. Lu, *Direct measurement of folding angle and strain vector in atomically thin WS₂ using second-harmonic generation*, *ACS Nano* **14**, 15806 (2020).
- [26] Y. W. Ho, H. G. Rosa, I. Verzhbitskiy, M. J. L. F. Rodrigues, T. Taniguchi, K. Watanabe, G. Eda, V. M. Pereira, and J. C. Viana-Gomes, *Measuring valley polarization in two-dimensional materials with second-harmonic spectroscopy*, *ACS Photonics* **7**, 925 (2020).
- [27] T. Heinz, in *Modern Problems in Condensed Matter Sciences* (Elsevier, 1991) pp. 353–416.
- [28] M. Fiebig, D. Fröhlich, S. Leute, and R. V. Pisarev, *Second harmonic spectroscopy and control of domain size in antiferromagnetic YMnO₃*, *Journal of Applied Physics* **83**, 6560 (1998).
- [29] S. Shree, I. Paradisanos, X. Marie, C. Robert, and B. Urbaszek, *Guide to optical spectroscopy of layered semiconductors*, *Nature Reviews Physics* **3**, 39 (2020).
- [30] M. Fiebig, V. V. Pavlov, and R. V. Pisarev, *Second-harmonic generation as a tool for studying electronic and magnetic structures of crystals: review*, *Journal of the Optical Society of America B* **22**, 96 (2005).
- [31] H. Ma, J. Liang, H. Hong, K. Liu, D. Zou, M. Wu, and K. Liu, *Rich information on 2d materials revealed by optical second harmonic generation*, *Nanoscale* **12**, 22891 (2020).
- [32] Y. Li, Y. Rao, K. F. Mak, Y. You, S. Wang, C. R. Dean, and T. F. Heinz, *Probing symmetry properties of few-layer MoS₂ and h-BN by optical second-harmonic generation*, *Nano Letters* **13**, 3329 (2013).
- [33] R. Yu, J. D. Cox, and F. J. G. de Abajo, *Nonlinear plasmonic sensing with nanographene*, *Physical Review Letters* **117**, 123904 (2016).
- [34] T. O. Wehling, A. Huber, A. I. Lichtenstein, and M. I. Katsnelson, *Probing of valley polarization in graphene via optical second-harmonic generation*, *Physical Review B* **91**, 041404 (2015).
- [35] F. Hipolito and V. M. Pereira, *Second harmonic spectroscopy to optically detect valley polarization in 2d materials*, *2D Materials* **4**, 021027 (2017).
- [36] X. Zhou, J. Cheng, Y. Zhou, T. Cao, H. Hong, Z. Liao, S. Wu, H. Peng, K. Liu, and D. Yu, *Strong second-harmonic generation in atomic layered GaSe*, *Journal of the American Chemical Society* **137**, 7994 (2015).
- [37] K. F. Mak, C. Lee, J. Hone, J. Shan, and T. F. Heinz, *Atomically thin mos₂: A new direct-gap semiconductor*, *Phys. Rev. Lett.* **105**, 136805 (2010).
- [38] A. Splendiani, L. Sun, Y. Zhang, T. Li, J. Kim, C.-Y. Chim, G. Galli, and F. Wang, *Emerging photoluminescence in monolayer mos₂*, *Nano Letters* **10**, 1271 (2010).
- [39] A. Chernikov, T. C. Berkelbach, H. M. Hill, A. Rigosi, Y. Li, O. B. Aslan, D. R. Reichman, M. S. Hybertsen, and T. F. Heinz, *Exciton binding energy and nonhydrogenic rydberg series in MonolayerWS₂*, *Physical Review Letters* **113**, 076802 (2014).
- [40] K. L. Seyler, J. R. Schaibley, P. Gong, P. Rivera, A. M. Jones, S. Wu, J. Yan, D. G. Mandrus, W. Yao, and X. Xu, *Electrical control of second-harmonic generation in a WSe₂ monolayer transistor*, *Nature Nanotechnology* **10**, 407 (2015).
- [41] G. Wang, X. Marie, I. Gerber, T. Amand, D. Lagarde, L. Bouet, M. Vidal, A. Balocchi, and B. Urbaszek, *Giant enhancement of the optical second-harmonic emission of WSe₂ monolayers by laser excitation at exciton resonances*, *Physical Review Letters* **114**, 097403 (2015).
- [42] G. Wang, A. Chernikov, M. M. Glazov, T. F. Heinz, X. Marie, T. Amand, and B. Urbaszek, *Colloquium: Excitons in atomically thin transition metal dichalcogenides*, *Reviews of Modern Physics* **90**, 021001 (2018).
- [43] T. Cheiwchanchamnangij and W. R. L. Lambrecht, *Quasiparticle band structure calculation of monolayer, bilayer, and bulk mos₂*, *Phys. Rev. B* **85**, 205302 (2012).
- [44] A. Ramasubramaniam, *Large excitonic effects in monolayers of molybdenum and tungsten dichalcogenides*, *Phys. Rev. B* **86**, 115409 (2012).
- [45] D. Y. Qiu, F. H. da Jornada, and S. G. Louie, *Optical spectrum of MoS₂: Many-body effects and diversity of exciton states*, *Phys. Rev. Lett.* **111**, 216805 (2013).
- [46] T. C. Berkelbach, M. S. Hybertsen, and D. R. Reichman, *Theory of neutral and charged excitons in monolayer transition metal dichalcogenides*, *Phys. Rev. B* **88**, 045318 (2013).
- [47] D. Y. Qiu, T. Cao, and S. G. Louie, *Nonanalyticity, valley quantum phases, and lightlike exciton dispersion in monolayer transition metal dichalcogenides: Theory and first-principles calculations*, *Phys. Rev. Lett.* **115**, 176801 (2015).
- [48] Y. V. Zhumagulov, A. Vagov, N. Y. Senkevich, D. R. Gulevich, and V. Perebeinos, *Three-particle states and brightening of intervalley excitons in a doped MoS₂ monolayer*, *Physical Review B* **101**, 245433 (2020).
- [49] Y. V. Zhumagulov, A. Vagov, D. R. Gulevich, P. E. F. Junior, and V. Perebeinos, *Trion induced photoluminescence of a doped MoS₂ monolayer*, *The Journal of Chemical Physics* **153**, 044132 (2020).
- [50] Y. V. Zhumagulov, A. Vagov, D. R. Gulevich, and V. Perebeinos, *Electrostatic control of the trion fine structure in transition metal dichalcogenide monolayers* (2021), [arXiv:2104.11800](https://arxiv.org/abs/2104.11800).
- [51] M. L. Trolle, G. Seifert, and T. G. Pedersen, *Theory of excitonic second-harmonic generation in monolayer-MoS₂*, *Physical Review B* **89**, 235410 (2014).
- [52] M. Kolos, L. Cigarini, R. Verma, F. Karlický, and S. Bhattacharya, *Giant linear and nonlinear excitonic responses in an atomically thin indirect semiconductor nitrogen phosphide*, *The Journal of Physical Chemistry C* **125**, 12738 (2021).
- [53] M. Richter and A. Knorr, *A time convolution less density matrix approach to the nonlinear optical response of a coupled system–bath complex*, *Annals of Physics* **325**, 711 (2010).
- [54] V. M. Axt and T. Kuhn, *Femtosecond spectroscopy in semiconductors: a key to coherences, correlations and quantum kinetics*, *Reports on Progress in Physics* **67**, 433 (2004).
- [55] D. Xiao, G.-B. Liu, W. Feng, X. Xu, and W. Yao, *Coupled spin and valley physics in monolayers of MoS₂ and other group-VI dichalcogenides*, *Phys. Rev. Lett.* **108**, 196802 (2012).
- [56] A. Kormányos, V. Zólyomi, N. D. Drummond, P. Rakyta, G. Burkard, and V. I. Fal'ko, *Monolayer MoS₂: Trigonal warping, the gamma valley, and spin-orbit coupling effects*, *Physical Review B* **88**, 045416 (2013).
- [57] A. Kormányos, G. Burkard, M. Gmitra, J. Fabian, V. Zólyomi, N. D. Drummond, and V. Fal'ko, *k-p theory for two-dimensional transition metal dichalcogenide semiconductors*, *2D Mater.* **2**, 022001 (2015).

- [58] A. Taghizadeh and T. G. Pedersen, *Nonlinear optical selection rules of excitons in monolayer transition metal dichalcogenides*, [Physical Review B](#) **99**, 235433 (2019).
- [59] Y. Cho and T. C. Berkelbach, *Environmentally sensitive theory of electronic and optical transitions in atomically thin semiconductors*, [Phys. Rev. B](#) **97**, 041409(R) (2018).
- [60] K. Zollner, P. E. Faria Junior, and J. Fabian, *Strain-tunable orbital, spin-orbit, and optical properties of monolayer transition-metal dichalcogenides*, [Phys. Rev. B](#) **100**, 195126 (2019).
- [61] A. Laturia, M. L. V. de Put, and W. G. Vandenberghe, *Dielectric properties of hexagonal boron nitride and transition metal dichalcogenides: from monolayer to bulk*, [npj 2D Materials and Applications](#) **2**, 6 (2018).
- [62] C. Zhang, C. Gong, Y. Nie, K.-A. Min, C. Liang, Y. J. Oh, H. Zhang, W. Wang, S. Hong, L. Colombo, R. M. Wallace, and K. Cho, *Systematic study of electronic structure and band alignment of monolayer transition metal dichalcogenides in van der waals heterostructures*, [2D Materials](#) **4**, 015026 (2016).
- [63] M. Rohlfing and S. G. Louie, *Electron-hole excitations and optical spectra from first principles*, [Phys. Rev. B](#) **62**, 4927 (2000).
- [64] N. S. Rytova, *The screened potential of a point charge in a thin film*, [Moscow University Physics Bulletin](#) **3**, 18 (1967).
- [65] L. V. Keldysh, *Coulomb interaction in thin semiconductor and semimetal films*, [Soviet Journal of Experimental and Theoretical Physics Letters](#) **29**, 658 (1979).
- [66] J. Johansson, P. Nation, and F. Nori, *QuTiP: An open-source python framework for the dynamics of open quantum systems*, [Computer Physics Communications](#) **183**, 1760 (2012).
- [67] J. Johansson, P. Nation, and F. Nori, *QuTiP 2: A python framework for the dynamics of open quantum systems*, [Computer Physics Communications](#) **184**, 1234 (2013).